Optimization of the wake oscillator for transversal VIV.

KURUSHINA, V., POSTNIKOV, A., FRANZINI, G.R. and PAVLOVSKAIA, E.

2022

Article

Optimization of the Wake Oscillator for Transversal VIV

Victoria Kurushina [1,2,*], Andrey Postnikov [3], Guilherme Rosa Franzini [4] and Ekaterina Pavlovskaia [5]

1   Marine, Offshore and Subsea Technology Group, School of Engineering, Newcastle University, Newcastle upon Tyne NE1 7RU, UK
2   Laboratory of Vibration and Hydrodynamics Modelling, Industrial University of Tyumen, 625000 Tyumen, Russia
3   Department of Civil, Environmental and Geomatic Engineering, University College London, London WC1E 6BT, UK; a.postnikov@ucl.ac.uk
4   Offshore Mechanics Laboratory, Escola Politécnica, University of São Paulo, São Paulo 03178-200, Brazil; gfranzini@usp.br
5   Centre for Applied Dynamics Research, School of Engineering, University of Aberdeen, Aberdeen AB24 3FX, UK; e.pavlovskaia@abdn.ac.uk
*   Correspondence: v.kurushina@outlook.com

Abstract: Vibrations of slender structures associated with the external flow present a design challenge for the energy production systems placed in the marine environment. The current study explores the accuracy of the semi-empirical wake oscillator models for vortex-induced vibrations (VIV) based on the optimization of (a) the damping term and (b) empirical coefficients in the fluid equation. This work investigates the effect of ten fluid damping variations, from the classic van der Pol to more sophisticated fifth-order terms, and prediction of the simplified case of the VIV of transversally oscillating rigid structures provides an opportunity for an extended, comprehensive comparison of the performance of tuned models. A constrained nonlinear minimization algorithm in MATLAB is applied to calibrate considered models using the published experimental data, and the weighted objective function is formulated for three different mass ratios. Comparison with several sources of published experimental data for cross-flow oscillations confirms the model accuracy in the mass ratio range. The study indicates the advantageous performance of the models tuned with the medium mass ratio data and highlights some advantages of the Krenk–Nielsen wake oscillator.

Keywords: vortex-induced vibrations; VIV; wake oscillator; phenomenological model; rigid structures; transversal oscillations

1. Introduction

In the vortex shedding phenomenon, fluid forces fluctuations and the resulting vibration have to be accounted for in the design of offshore structures. Specific attention to this aspect should be assigned when slender objects are considered which may comprise supports, suspensions, tethers, cables, umbilicals or pipelines, submerged or hanging in the air. Their geometrical configuration, mass, damping and frequency and the velocity profile of the fluid flow define the development of a possible lock-in condition, with vibration of a high frequency, amplitude and speed. For complex systems, it is important to avoid the vortex-induced vibration (VIV), in order to delay the accumulation of the associated structural fatigue.

The periodicity of hydrodynamic forces, changes to their time history subject to lock-in condition, as well as the self-limiting and self-exciting nature of free vibration, may be qualitatively captured using a wake oscillator, an approach proposed in [1]. Further improvement of wake oscillators is presented in [2,3], where the application of Rayleigh, van der Pol and fifth-order damping terms is discussed. The study in [2] considers the use of three empirical constants in the fluid equation: a fluid damping parameter aimed to determine the occurrence of lock-in, the second coefficient introduced in the cubic stiffness

term to model the size of the displacement lock-in peak and the third coefficient defined as the relationship of the previous two and incorporated in the velocity coupling term. This model for VIV in the air [2] was further modified for flexible structures and different boundary conditions, and proved its applicability to predict transversal oscillations for a range of parameters [4]. It has been suggested that the empirical coefficients used should vary with the initial lift coefficients applied for modelling. However, the question of alternation of the damping terms in the fluid oscillator and tuning of the empirical constants has not been answered in detail.

Wake oscillator models have been gradually improved in the late XX century and at the beginning of the XXI century. The nonlinear structural equation has been considered in [5], while the model still required recalibration of empirical constants for separate cases of published experimental data. Variations of damping terms in the fluid equation were proposed in [6–8]. Values of empirical constants were discussed in [9,10]. Preference for the acceleration coupling term was proved in [11], and the use of nonlinear coupling and frequency-dependent coefficients to facilitate modelling of both free and forced vibrations has been pursued in [12–14]. The use of a single fluid oscillator for rigid cylinders mounted on elastic supports that allow displacements on the horizontal plane (2DOF) based on the relationship between the drag and lift coefficients was discussed in [15], and developed in [16,17]. Additionally, the relationship of the drag coefficient to the oscillation amplitude and the flow velocity, and also possible patterns embedded in the damping constant of the fluid oscillator were discussed in [18–20].

Despite substantial improvements and insight into the nature of the fascinating vortex-induced vibration phenomenon, its remarkable sensitivity to the exact conditions of the external environments still poses challenges to simulations, starting with the simplified transversal oscillations. Published experimental data in [21] present the case for the observed differences in the VIV lock-in development for the one degree-of-freedom (1DOF) rigid cylinder, related to changes in the distance of the end of structure from the wall. The formation of a minor vortex at one end of the structure has been able to alter the lock-in displacement record and created difficulties for prediction tools. The specific challenge indicated in this paper is in the prediction of the lock-in occurrence that moved to a different flow velocity.

The systematic experimental study [18] reports similar changes in the position of the initial lock-in branch for 1DOF and 2DOF rigid structures related to the value of the mass ratio. Here, an increasing mass ratio delays the resonance occurrence in the reduced velocity range. The theoretical study in [22], based on these data, shows that the lock-in start for a 2DOF rigid structure is similar for a few different experimental arrangements [5,18,23–25] for approximately the same mass ratio, and can be captured by tuning the empirical constants, including the coefficient correcting the lock-in start. A similar approach has been taken in [8,26–28] in order to consider the impact of both empirical constants and damping terms in the wake oscillator equations on the possible accuracy of VIV predictions.

Based on the knowledge and previous results available in the published literature refs. [8,22,26,27], the current study attempts to eliminate the gap in understanding the accuracy of transversal VIV wake oscillators by taking a systematic approach to optimization and comparison of models of semi-empirical nature. For this purpose, the mathematical formulation of the 1DOF case studied in [11,19,29] is improved by the introduction of the damping terms considered in [28] and an additional four extended damping formulations, in order to optimize the qualitative description of the lock-in behaviour. The calibration program in this research is designed in a more comprehensive manner than the previous attempts to optimize models for a single case, as in [22,27]. The present optimization is performed on the basis of published data in [18] for three cases of transversal oscillations with a different mass ratio. Three selected mass ratios can be defined as "low", "medium" and "high", according to the authors of [25,30] where the mass ratio is related to features of observed lock-in branches. Performance for these three groups of optimized models is intended to provide convincing arguments towards particular suitability of certain damping

terms and efficient optimization strategies, as well as a realistic view on the application ranges for tuned semi-empirical models.

The paper is organized as follows. Section 1 provides a theoretical background. Section 2 introduces the basic mathematical model of transversal VIV for a rigid elastically mounted structure and changes related to the fluid damping optimization. Section 3 gives details of the nonlinear optimization to find values of suitable empirical parameters for the models with a distinct damping term. Comparison of the tuned models with published experimental data and a comprehensive discussion on their suitability is included in Section 4. Concluding remarks on the main findings are given in Section 5.

2. Optimization of Mathematical Model

The basic mathematical model of a one degree-of-freedom elastically supported cylinder experiencing VIV is selected for this research and has been previously studied in [11,29]. The system under consideration is presented in Figure 1, and the structure is subject to free cross-flow vibration only under the influence of the uniform flow. The homogeneous cylinder has a length L, diameter D and has a constant circular cross-section. The structure is characterized with the mass per unit length m_s, r_s and k are the damping coefficient and stiffness of elastic support, and only the motion in the cross-flow ($\overline{Y}$) direction is allowed.
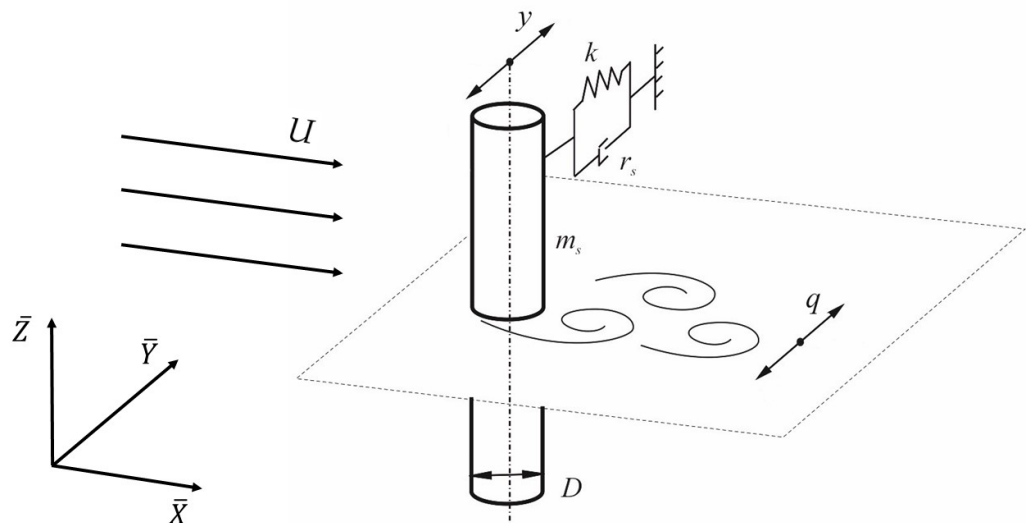
Figure 1. One degree-of-freedom elastically supported rigid structure interacting with the uniform flow of velocity U.

The mathematical description of this system and the VIV phenomenon, in general, involves the following non-dimensional quantities, characterizing the development of the lock-in condition:

$$\omega_{st} = \frac{\omega_n}{\omega_0}; \quad \xi = \frac{r_s}{2\omega_0 m_*}; \quad \mu = \frac{4m_s}{\pi \rho_f D^2}, \tag{1}$$

where ω_n is the natural frequency of the structure defined as $\omega_n = \sqrt{\frac{k}{m_*}}$, ω_0 is the reference frequency assumed in this study equal to the natural frequency of the rigid structure, ρ_f is the fluid density, ξ is the non-dimensional damping ratio, ω_{st} is the non-dimensional natural frequency of the structure and μ is the mass ratio. Mass per unit length m_* includes the structural mass and fluid added mass, where C_A is the potential fluid added mass coefficient:

$$m_* = \left(\mu + C_A\right)\frac{\pi \rho_f D^2}{4}. \tag{2}$$

The current study follows the approach taken in [22] to identify the value of the fluid added mass coefficient based on the calibration with published experimental data, instead of the traditionally used $C_A = 1$. The calibration approach allows tuning C_A in order to capture the lock-in peak record of the structural displacement against reduced velocity in a more accurate manner both quantitatively and qualitatively, by changing the shape of the upper branch. For brevity, the reference frequency ω_0 is assigned equal to the natural frequency of the structure ω_n in this work, therefore, the non-dimensional frequency is $\omega_{st} = \frac{\omega_n}{\omega_0} = 1$ for all results demonstrated later in Section 3.

Time t and cross-flow displacement y of the centre of the structure are nondimensionalized as τ and Y respectively, using already introduced parameters:

$$\tau = \omega_0 t; \quad Y = \frac{y}{D}. \tag{3}$$

The uniform fluid flow is presented in the model as a velocity U and vortex shedding frequency Ω_f, or, in the non-dimensional form, the reduced velocity U_R and vortex shedding frequency Ω_R as follows:

$$U_R = \frac{2\pi U}{\omega_n D}; \quad \Omega_R = \frac{\Omega_f}{\omega_0} = \frac{2\pi St U}{\omega_0 D}. \tag{4}$$

In this work, all calculations are performed for the reduced velocity from the published experimental data. The Strouhal number St is assumed to be constant and equal to 0.2 for all considered cases, following the work in [31]. The lift and drag forces acting on the cylinder are calculated using the fluctuating lift and drag coefficients C_L and C_D^{fl}. The fluctuating drag C_D^{fl} is a difference of drag coefficient C_D of a moving structure and drag coefficient C_{D0} of a stationary structure, or $C_D^{fl} = C_D - C_{D0}$, and here, the coefficients C_{L0} and C_{D0}^{fl} characterize the lift and fluctuating drag coefficient amplitudes of a stationary structure respectively. In general, the fluctuating nature of the lift and drag coefficients during the vibration with respect to their values for a stationary structure is quantified using the non-dimensional cross-flow q wake coefficient:

$$q = \frac{2C_L}{C_{L0}}. \tag{5}$$

The full nondimensional model involved in this research [11,29] provides the estimates for the structural dynamics Y in the cross-flow plane only and the respective fluctuations of the non-dimensional component of the lift force q:

$$\ddot{Y} + 2\xi\dot{Y} + \omega_{st}^2 Y = d(\Omega_R - KSt)^2 q - e(\Omega_R - KSt)\dot{Y}; \tag{6}$$

$$\ddot{q} + \varepsilon_y(\Omega_R - KSt)(q^2 - 1)\dot{q} + (\Omega_R - KSt)^2 q = A_y \ddot{Y}, \tag{7}$$

where A_y stands for the coupling constant, K represents the calibrated constant of the lock-in occurrence, as introduced in [22], ε_y is the wake oscillator damping coefficient, and non-dimensional coefficients involved in the force balance defining the structural motion are:

$$d = \frac{C_{L0}\rho_f D^2}{16\pi^2 St^2 m_*}; \quad e = \frac{C_{D0}\rho_f D^2}{4\pi St m_*}. \tag{8}$$

Following the approach taken in [22,27,28], optimization of the wake oscillator in Equation (7) is performed by the introduction of damping terms proposed in [3,6], including the use of separate constants ε_y for the models with modified Rayleigh and modified van der Pol oscillators. Table 1 summarizes all mathematical alternatives of the wake oscillator equations considered in this research. The current work, first of all, expands the analysis in [28] towards a comprehensive calibration study, where all empirical constants in the oscillator equation from Table 1 are tuned with low, medium and high mass ratio cases

respectively, and, hence, form three separate groups of optimized models demonstrating the lowest of objective functions. Definitions of objective functions are discussed in more detail in Section 3. These models are further compared in Section 4 to each other by their predictions against the published experimental data for the cross-flow displacement amplitudes observed during the lock-in in several cases [18,32–34].

The second important improvement of the wake oscillator damping in this study is an attempt to introduce multiple damping terms comprising a combination of $q^p \dot{q}^m$, where the powers p and m vary from 0 to 5, the contribution of each term is governed by a separately calibrated constant ε_y. These equations are labeled as "Oscillator-1", "Oscillator-2", "Oscillator-3" and "Oscillator-4" and contain the optimized constants ε_{y1} to ε_{y15}. The approach to optimization of constants involved in the system of equations in Equations (6) and (7) and all wake oscillator alternatives in Table 1 is presented in the next section.

Table 1. Wake oscillator equations.

Oscillator	Cross-Flow Equation
Classic van der Pol	$\ddot{q} + \varepsilon_y \Omega_R \dot{q} q^2 - \varepsilon_y \Omega_R \dot{q} + \Omega_R^2 q = A_y \ddot{Y};$
Modified van der Pol	$\ddot{q} + \varepsilon_{y1} \Omega_R \dot{q} q^2 - \varepsilon_{y2} \Omega_R \dot{q} + \Omega_R^2 q = A_y \ddot{Y};$
Classic Rayleigh	$\ddot{q} - \varepsilon_y \Omega_R \dot{q} + \frac{\varepsilon_y}{\Omega_R} \dot{q}^3 + \Omega_R^2 q = A_y \ddot{Y};$
Modified Rayleigh	$\ddot{q} - \varepsilon_{y1} \Omega_R \dot{q} + \frac{\varepsilon_{y2}}{\Omega_R} \dot{q}^3 + \Omega_R^2 q = A_y \ddot{Y};$
Landl	$\ddot{q} + \Omega_R \dot{q} (\varepsilon_{y1} - \varepsilon_{y2} q^2 + \varepsilon_{y3} q^4) + \Omega_R^2 q = A_y \ddot{Y};$
Krenk–Nielsen	$\ddot{q} - \varepsilon_{y1} \Omega_R \dot{q} + \varepsilon_{y2} \Omega_R \dot{q} q^2 + \frac{\varepsilon_{y3}}{\Omega_R} \dot{q}^3 + \Omega_R^2 q = A_y \ddot{Y};$
Oscillator-1	$\ddot{q} + (-\varepsilon_{y1} \Omega_R + \varepsilon_{y2} \Omega_R q^2 + \varepsilon_{y3} \dot{q} + \varepsilon_{y4} \Omega_R q) \dot{q} +$ $(\varepsilon_{y5} + \varepsilon_{y6} q + 1) \Omega_R^2 q = A_y \ddot{Y};$
Oscillator-2	$\ddot{q} + (-\varepsilon_{y1} \Omega_R + \varepsilon_{y2} \Omega_R q^2 + \varepsilon_{y3} \dot{q} + \varepsilon_{y4} \Omega_R q + \varepsilon_{y7} \dot{q} q +$ $+ \varepsilon_{y8} \frac{\dot{q}^2}{\Omega_R}) \dot{q} + (\varepsilon_{y5} + \varepsilon_{y6} q + \varepsilon_{y9} q^2 + 1) \Omega_R^2 q = A_y \ddot{Y}$
Oscillator-3	$\ddot{q} + (-\varepsilon_{y1} \Omega_R + \varepsilon_{y2} \Omega_R q^2 + \varepsilon_{y3} \dot{q} + \varepsilon_{y4} \Omega_R q + \varepsilon_{y7} \dot{q} q +$ $+ \varepsilon_{y8} \frac{\dot{q}^2}{\Omega_R} + \varepsilon_{y11} \frac{\dot{q}^3}{\Omega_R^2} + \varepsilon_{y12} \frac{q \dot{q}^2}{\Omega_R} + \varepsilon_{y13} q^3 \Omega_R + \varepsilon_{y14} q^2 \dot{q}) \dot{q} +$ $+ (\varepsilon_{y5} + \varepsilon_{y6} q + \varepsilon_{y9} q^2 + \varepsilon_{y10} q^3 + 1) \Omega_R^2 q = A_y \ddot{Y};$
Oscillator-4	$\ddot{q} + (-\varepsilon_{y1} \Omega_R + \varepsilon_{y2} \Omega_R q^2 + \varepsilon_{y3} \dot{q} + \varepsilon_{y4} \Omega_R q + \varepsilon_{y7} \dot{q} q +$ $+ \varepsilon_{y8} \frac{\dot{q}^2}{\Omega_R} + \varepsilon_{y11} \frac{\dot{q}^3}{\Omega_R^2} + \varepsilon_{y12} \frac{q \dot{q}^2}{\Omega_R} + \varepsilon_{y13} q^3 \Omega_R + \varepsilon_{y14} q^2 \dot{q} +$ $+ \varepsilon_{y16} \frac{\dot{q}^4}{\Omega_R^3} + \varepsilon_{y17} q^4 \Omega_R + \varepsilon_{y18} \frac{q \dot{q}^3}{\Omega_R^2} + \varepsilon_{y19} q^3 \dot{q} + \varepsilon_{y20} \frac{q^2 \dot{q}^2}{\Omega_R}) \dot{q}$ $+ (\varepsilon_{y5} + \varepsilon_{y6} q + \varepsilon_{y9} q^2 + \varepsilon_{y10} q^3 + \varepsilon_{y15} q^4 + 1) \Omega_R^2 q = A_y \ddot{Y}$

## 3. Optimization of Empirical Coefficients

Calibration of the considered models is performed using the experimental data [18] for displacement amplitudes (half of the average of the 10 highest peak-to-peak values) over the range of reduced velocities. In these data, 20 to 26 available points are associated with the expected lock-in velocity range defined by the proximity of frequencies of the oscillating structure and the vortex shedding process. The involved data are presented in detail in Table 2, and three sets of the lock-in data for three distinct mass ratios of 2.36, 6.54 and 10.63 are used in this research for calibration of empirical coefficients. According to [25,35], these mass ratios could be referred to as "low", "medium" and "high". Other available experimental data [18] are used in this research to validate modified models calibrated with these mass ratios.

The wake oscillator model solution is generally obtained with the MATLAB ode45 solver with the non-dimensional time step of 0.2 and initial conditions of $Y = \dot{Y} = \dot{q} = 0$, $q = 0.1$, so that the structure is assumed to be at rest at the start of the simulation. The rigid structure experiences temporary unstable oscillations with the further stabilization of the

limit cycle, and the displacement is calculated from the signal with a built-in MATLAB statistical function for the period of stable vibration.

The calibration in this work employs the general idea of the objective function presented in [22], with the preference for capturing the maximum amplitude of the lock-in peak and the lock-in bandwidth in the reduced velocity range. This is reflected in the distribution of the data points, used to define the objective function, across the lock-in peak in Figure 2. Optimization of empirical parameters, outlined in Section 2, is conducted using the constrained nonlinear minimization from the MATLAB Optimization Toolbox. The objective function is designed based on the selected N data points from the available set [18] distributed along the initial, upper and lower branches of the lock-in peak, as displayed in Figure 2. The procedure involves in total of $N = 8$ out of the 26 available experimental data points for the mass ratio of 2.36, and $N = 9$ out of the 26 data points for the mass ratios of 6.54 and 10.63 [18].

The errors with experimental data are computed using a sum of absolute or relative errors for the standard deviation $std()$ or the maximum $max()$ of the amplitude of the displacement signal Y generated by each model. Four objective function definitions are presented in Table 3. For the purpose of defining the objective function S, the modelled displacement amplitude for the control point i is denoted in Table 3 as Y_{mi}, and Y_{exp_i} is the experimental value at the appropriate reduced velocity. The weighting coefficient w_i in Table 3 defines the contribution of the error registered in the point i and takes the value of 1, 2, 3 or 4, depending on the point location on the lock-in peak, as shown in Figure 2. Grey points in Figure 2 are not involved in the optimization procedure. Use of the standard deviation of the displacement signal to be calibrated with the signal statistics in [18] allows for a reasonable safety gap to be embedded in the model results, while generally capturing the peak shape. Further optimization settings, including coefficients' initial values and value constraints, are given in Appendix A, and some specific settings to the new multiple-terms oscillators are discussed in [36]. The results of the optimization are presented in Appendix B, and these models calibrated with the transversal displacement specifically demonstrate the advantageous accuracy, compared to the models selected in [22,27] when they are applied for the case of the cross-flow only VIV of rigid structures. For this reason, the Section 4 demonstrates the performance of the calibrated 1DOF rigid structure models, listed in Section 2.
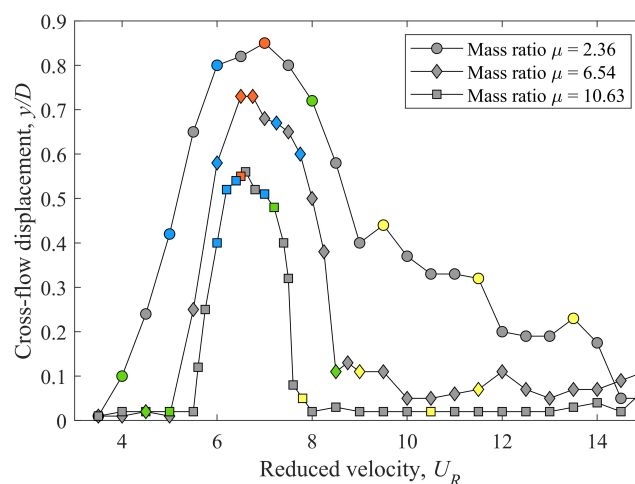
Figure 2. Illustration of the experimental points in the dataset for the mass ratios of 2.36, 6.54 and 10.63 [18] in terms of the reduced velocity and the registered displacement amplitude. Data points selected for the optimization procedure have the weights w_i equal to 4 (orange points), 3 (blue points), 2 (green points) and 1 (yellow points) in the objective function and generally hold an advantageous position to capture the lock-in peak shape.

Table 2. Case parameters of experimental data by Stappenbelt and Lalji (2008) [18], used for the calibration and as the first validation instance in the present study.

Parameter, Symbol (Units)	Value
Mass ratio, μ	2.36, 3.68, 5.19, 6.54, 7.91, 8.76, 10.63, 12.96
Damping ratio, ξ	0.006
Mass-damping ratio, $\mu\xi$	0.014, 0.022, 0.031, 0.039, 0.047, 0.053, 0.064, 0.078
Griffin mass-damping ratio, $(\mu + C_A)\xi$	0.020, 0.028, 0.037, 0.045, 0.053, 0.059, 0.070, 0.084
Maximum lock-in displacement amplitude, y/D	0.85, 0.80, 0.74, 0.73, 0.68, 0.64, 0.56, 0.43
Diameter, D (m)	0.0554
Aspect ratio, L/D	8
Natural frequency, f_n (Hz)	1.711, 1.502, 1.359, 1.261, 1.153, 1.151, 1.084, 1.025
Flow velocity interval, U (m/s)	0.33–1.52
Reynolds number interval, Re	18,300–83,800
Reduced velocity interval, U_R	3.5–16.0

Table 3. Four objective functions based on the experimental data for N control points, highlighted in Figure 2.

Number	Objective Function
CF 1	$S = \sum_{i=1}^{N} w_i (max(Y_{m_i}) - Y_{exp_i})^2$
CF 2	$S = \sum_{i=1}^{N} w_i \frac{|max(Y_{m_i}) - Y_{exp_i}|}{Y_{exp_i}}$
CF 3	$S = \sum_{i=1}^{N} w_i (std(Y_{m_i}) - Y_{exp_i})^2$
CF 4	$S = \sum_{i=1}^{N} w_i \frac{|std(Y_{m_i}) - Y_{exp_i}|}{Y_{exp_i}}$

4. Results and Discussion

In this work, the optimization of coefficients is performed for 10 models listed in Section 2, for 3 mass ratios studied in [18] using 4 objective functions in Section 3. The short list of tuned models with the optimized coefficients, given in Appendix B, and their performance against the published data from the original selected set-up [18] and other experimental series, described in Appendix C, is discussed in three subsections below, with respect to the mass ratio chosen for calibration.

4.1. Models Calibrated with Low Mass Ratio

The illustration of the optimization results is given in Figure 3a,b for the models in Appendix B calibrated with the low mass ratio data [18]. These models, with no changes in the optimized coefficients set, are further compared to the lock-in data recorded in [18] for the mass ratios of 3.68 and 5.19, and this comparison is shown in Figure 3c–f, respectively. Data in Figure 3 provide the evidence of the satisfactory performance of the models in the range of the mass ratio from 2 to 5 with the coefficient K from 0.75 to 1.22, which is consistent with the findings in [22] for the two degrees-of-freedom system. The models tuned for the low mass ratio demonstrate an approximately equal applicability of the van der Pol and Rayleigh damping terms for the transversally oscillating rigid structure, with no apparent advantage of the new extended oscillators from Table 1.
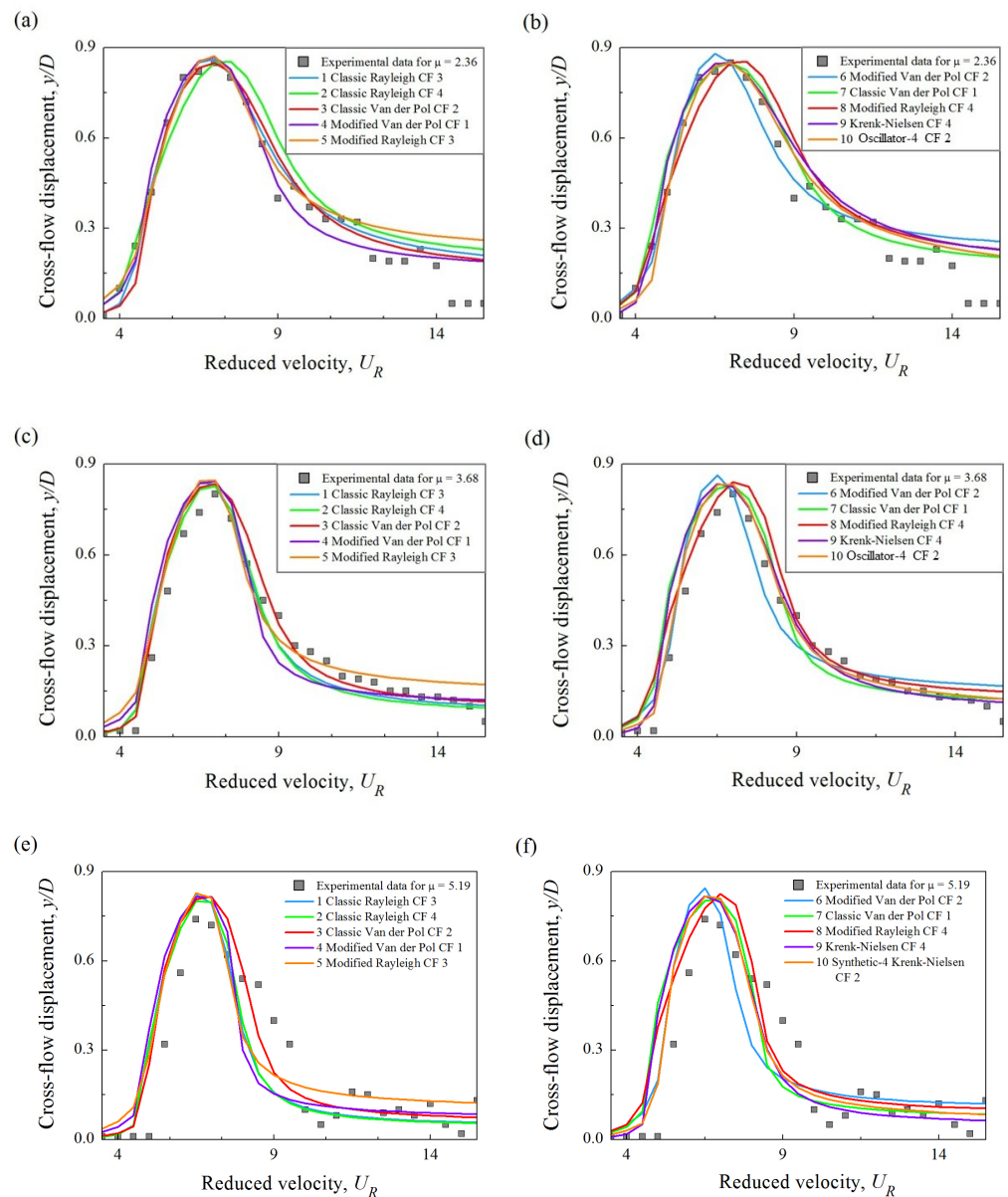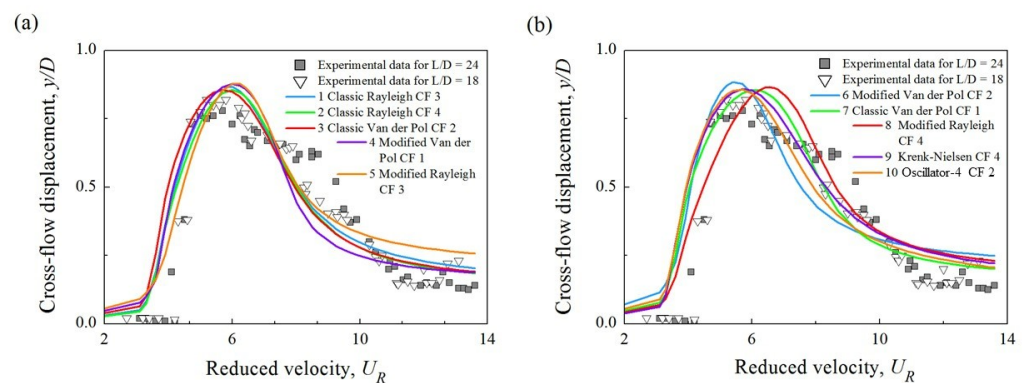
Figure 3. Cross-flow displacement amplitudes obtained by the one degree-of-freedom models in Appendix B, calibrated with the low mass ratio: calibration results for low mass ratio 2.36 for oscillators 1–5 (**a**) and 6–10 (**b**); validation results for mass ratio 3.68 for oscillators 1–5 (**c**) and 6–10 (**d**); validation results for mass ratio 5.19 for oscillators 1–5 (**e**) and oscillators 6–10 (**f**). Experimental data for calibration and validation from [18]. Damping ratio $\xi = 0.006$, Reynolds number range 18,300–83,800.

Generally, the models 1, 3, 4, 5, 7, 9 and 10 from the low mass ratio list in Appendix B provide a relatively safe and accurate fit for the upper branch in Figure 3a,b. Models 2, 7 and 8 allow a safer version of the initial branch, and models 2, 5, 8, 9 and 10 allow a safer version of the lower branch and following desynchronization region. Model 6 allows replication of the displacement amplitude at $U_R = 7.0$ which is the highest amplitude in the target experimental data, but it underestimates the width of the lock-in region, so, the fit is finally less advantageous than all others. Models 3, 8, 9 and 10 demonstrate more accurate predictions for the height and width of the lock-in peaks in Figure 3c–f when the mass ratio is increased to 3.68 and 5.19. The result in Figure 3 suggests that Model 3 with the van

der Pol damping and the objective function defined as CF 2 is most suitable for predicting dynamics in the set-up [18] in the interval μ = 2.0–5.0.

The same models provide suitable estimates of the maximum displacement amplitude for the cases considered in [33]. Comparison between the experimental data in [33] and [18] shows a visible difference between these published results: (a) in the slope of the initial branch, (b) slope of the lower branch and (c) a different location of the maximum displacement of the lock-in peak value in the reduced velocity range. From the comparison of the case parameters, given in Section 3 and Appendix C, these distinctions may originate from the difference in the considered aspect ratio of structures and the Reynolds number range. The model in Section 2 does not appear to have specific tools to account for this difference, except for the coefficient K that contributes to the vortex shedding frequency integrated into the fluid oscillator. For this reason, the coefficient K for the comparison with the data [33] in Figure 4 is assigned to 0. This allows appreciating the qualitative match of the tuned models with the lower aspect ratio data for $L/D = 18$, including the lock-in bandwidth, slopes and the upper branch, with minor advantages of one model over the others. The oscillators 1, 2, 3, 7, 9 and 10 may be seen as more advantageous in capturing these proportions. The data published in [33] for $L/D = 24$ show a different geometry of the lower branch height and width in the reduced velocity range, as well as smaller amplitudes of the upper branch so that the tuned models do not qualitatively capture this type of peak in general.
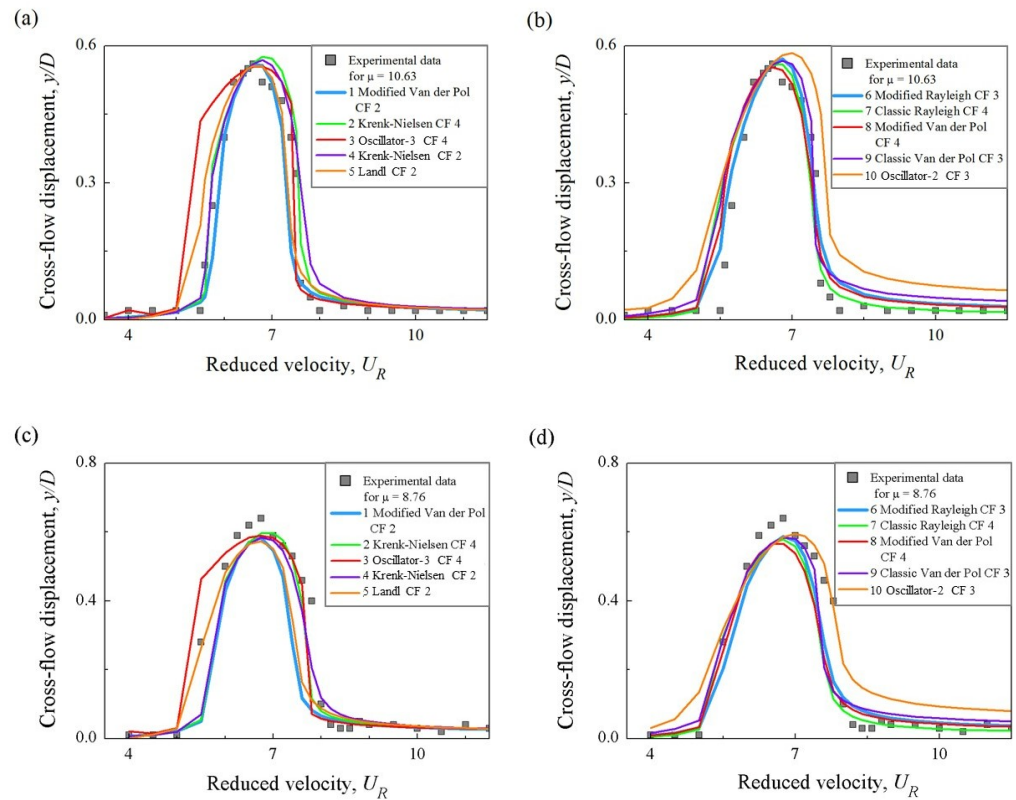

Figure 4. Cross-flow displacement amplitudes for the reduced velocity range generated by the models calibrated with low mass ratio with oscillators 1–5 (**a**) and oscillators 6–10 (**b**) from Appendix B, with $K = 0$. The experimental data for two aspect ratios are from the published results by the authors of [33] for the mass ratio 2.5, damping ratio ξ = 0.005, Reynolds number range 1320–6660.

4.2. Models Calibrated with High Mass Ratio

The comprehensive experimental data [18] for the one degree-of-freedom system demonstrate a rapid evolution of the lock-in occurrence when the mass ratio grows from 8 to 13. These evolving features include: (a) occurrence of the initial branch at a higher reduced velocity; (b) practical similarity to the cross-flow maximum amplitudes observed for the two degrees-of-freedom cases; (c) compression of the lower branch bandwidth in terms of the reduced velocity; (d) general reduction of the maximum peak height.

The following attempt has been made to calibrate the wake oscillator models in this range with the mass ratio 10.63, with the tuned coefficients provided in Appendix B, and the result of calibration shown in Figure 5a,b. As could be expected, the calibration appears to be successful for a number of models. The optimization result demonstrates the accuracy of mostly non-classic, modified oscillators in this range, including two oscillators with extended damping terms in the short list in Appendix B. Model 10 (Oscillator-2) may be considered as most applicable in this range. The coefficient K for the mass ratio of 10.63 varies from 1.10 to 2.32 which accounts for the delay in the occurrence of the initial branch in the reduced velocity range.

However, as could be expected from the qualitative description of the experimental data in [18] for the high mass ratio, the application range for these tuned models appears to be about from $\mu = 8.5$ to $\mu = 11.0$. The result of comparison for the mass ratio 8.79 is shown in Figure 5c,d and demonstrates underestimation of the amplitudes of the upper branch. The results for the mass ratio 12.96, not shown in this paper, in turn, show a substantial overestimation of the lock-in peak. The models calibrated with the high mass ratio also appear to be not applicable to predict the lock-in occurring in other experimental series.

Figure 5. Cross-flow displacement amplitudes obtained by the one degree-of-freedom models in Appendix B, calibrated with the high mass ratio: calibration results for high mass ratio 10.63 for oscillators 1–5 (**a**) and 6–10 (**b**); validation results for mass ratio 8.76 for oscillators 1–5 (**c**) and 6–10 (**d**). Experimental data for calibration and validation from [18]. Damping ratio $\xi = 0.006$, Reynolds number range 18,300–83,800.

4.3. Models Calibrated with Medium Mass Ratio

The last group of models in Appendix B have been selected based on the calibration with the medium mass ratio of 6.54 [18]. This group contains the Krenk–Nielsen, modified van der Pol, modified and classic Rayleigh equations and one oscillator with extended damping terms, that appear to be more accurate than the classic van der Pol equation, according to the minimal objective functions. This list of oscillators is clearly different from the other mass ratios. The coefficient K varies from 0.96 to 2.12 across these models, to indicate the initial branch position at a reduced velocity slightly higher than for the mass ratio of 2.36 and lower than for 10.63.

The calibration results for the medium mass ratio 6.54 are presented in Figure 6 and indicate a particular suitability of models 1, 2, 3, 4, 5, 6, 7 and 10. Model 8 and classic Rayleigh oscillators appear not applicable for the prediction of the left slope of the lock-in peak, while suitable for the prediction of other branches. Model 5 gives the most accurate highest displacement amplitudes and a correct slope of the initial branch, but prediction in the reduced velocity interval from 7.0 to 8.0 is disadvantageous. Models 7 and 10 may be considered as quite correct both qualitatively and quantitatively in this case.
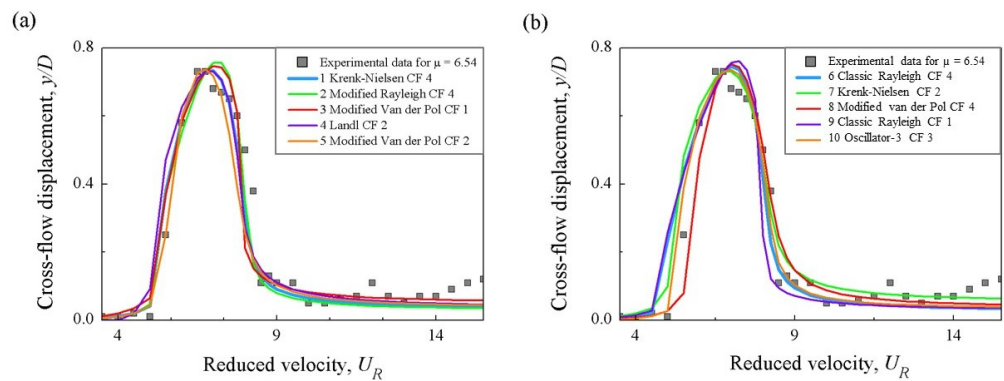
Figure 6. Cross-flow displacement amplitudes obtained by the one degree-of-freedom models in Appendix B, calibrated with the medium mass ratio 6.54 for oscillators 1–5 (**a**) and 6–10 (**b**). Experimental data for calibration and validation from [18]. Damping ratio $\xi = 0.006$, Reynolds number range 18,300–83,800.

The application of these optimized models for the mass ratio ranges from 2 to 5 and 7 to 11 [18] is shown in Figures 7–10, with no changes to the calibrated coefficients. Validation with the mass ratio 2.36 in Figure 7a,b demonstrates the correctly predicted bandwidth and some differences with the amplitudes in the upper branch. Models 4, 6, 7 and 9 may be recommended as more accurate, with some advantages demonstrated by models 6 and 7. The match of non-dimensional vibration frequencies indicated in the experiments [18] for the mass ratio 2.36 and non-dimensional frequencies of displacement signals ω_y generated by the models are illustrated in Figure 8a,b. Here, models 1 to 7 demonstrate an acceptable match with the experimental frequencies between $U_R = 3.0$ and $U_R = 9.0$, while the theoretical values exhibit a steeper increasing trend at $U_R > 9.0$. Modelling results for the mass ratio 6.54 in Figure 8c,d show a more narrow range of the frequency lock-in, consistent with the range of observed high displacement amplitudes.

Models 4, 6 and 7 well capture the lock-in bandwidth for the mass ratio 3.68, as shown in Figure 7c,d, while models 2, 3 and 9 can estimate the maximum displacement amplitude more correctly. Here, model 7 generally shows a better performance than the other models for the reduced velocity $U_R = 9.0$ and above.

The comparison of the tuned models with the mass ratio of 5.19 in Figure 7e,f demonstrates a general deviation of models from the experimental lower branch. Model 5 can be considered accurate for the predictions below $U_R = 8.0$, and model 7 captures the peak configuration relatively well, if the full range of U_R is considered.

A similar performance is recorded in Figure 9 for the experimental series [32] for a slightly increased damping ratio of 0.008. The minor change in the parametric set leads to a slightly wider lock-in range in terms of the reduced velocity and a pronounced jump in the amplitude between the lower and upper branches, especially for the mass ratio of 3.01. If the tuned models of this group are applied with no changes in the coefficients set, the lock-in occurrence appears to be predicted with a generally suitable accuracy for the mass ratio 3.01, with some advantages of Landl and classic Rayleigh oscillators, as shown in Figure 9a,b. All models in this group do not capture the amplitude drop between the upper and lower branches, and the coefficient K appears to be slightly higher than required for this arrangement.

The accuracy of these models for the mass ratio 5.19 in Figure 9c,d has a similarity to the results in Figure 7e,f in the way the lower branch of the lock-in is underestimated. Figure 9c,d also indicate an overprediction of the maximum amplitude of the response during the lock-in for a higher damping ratio in [32].
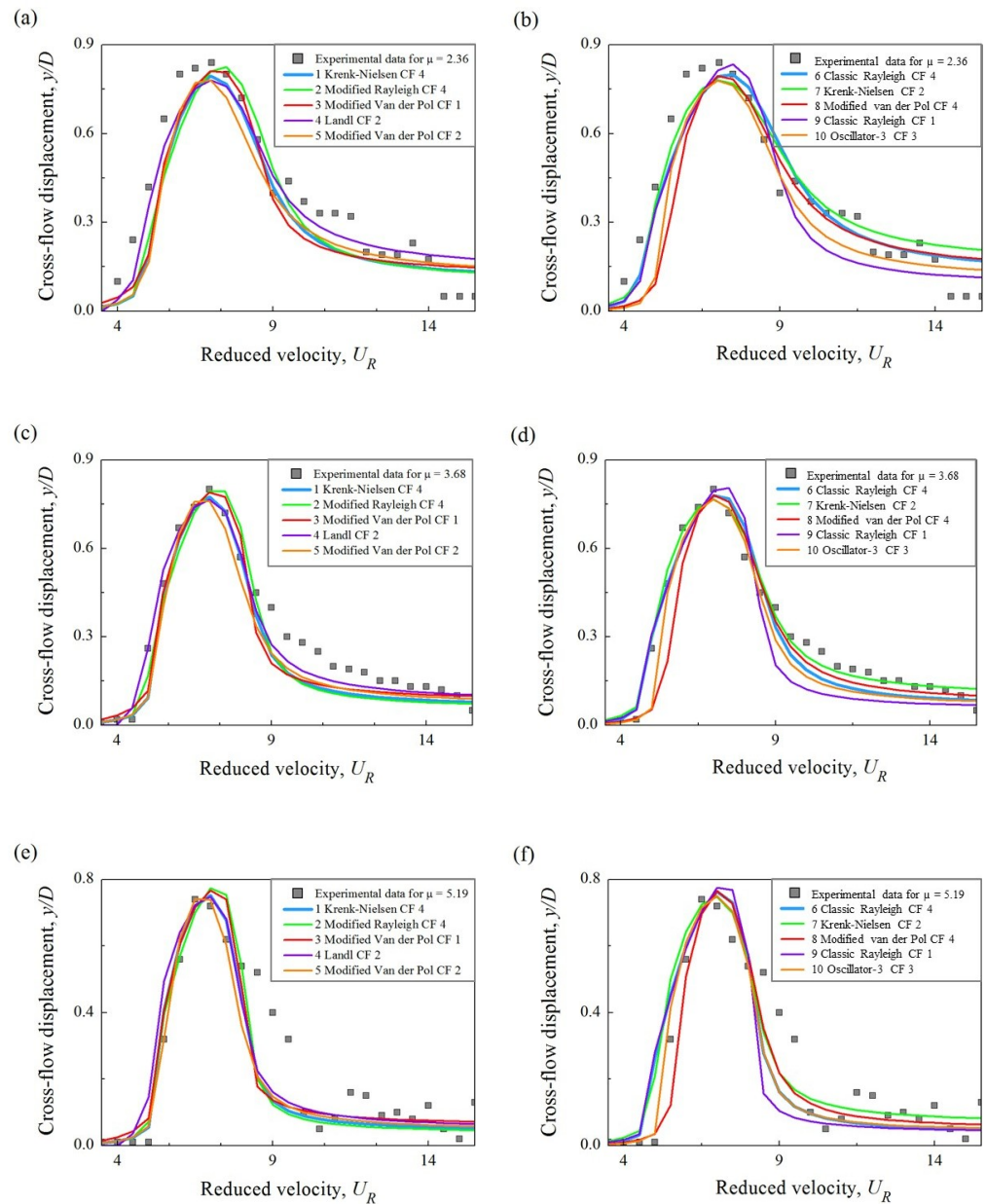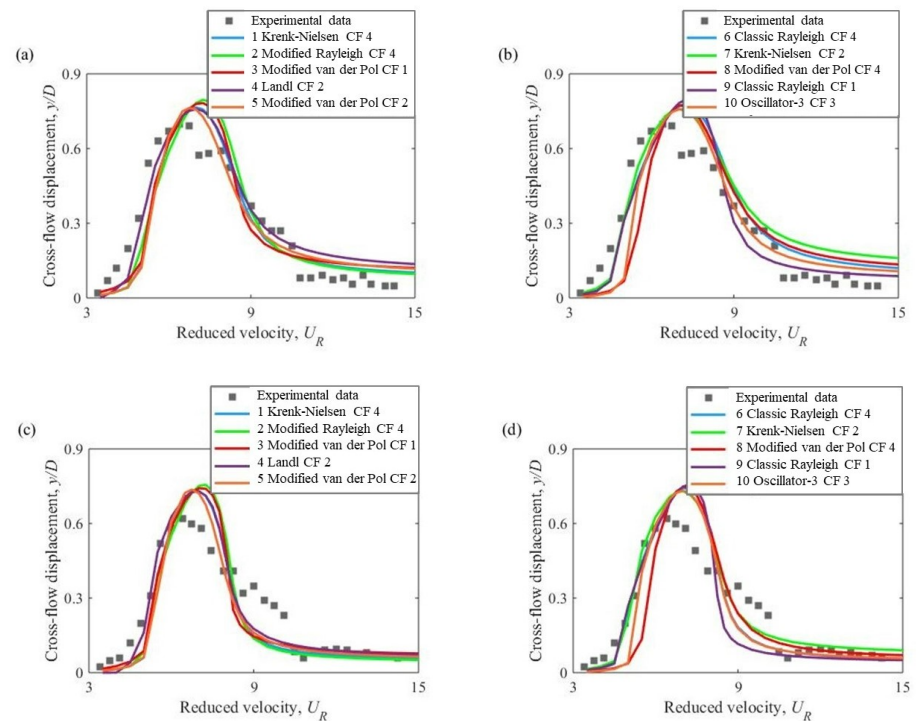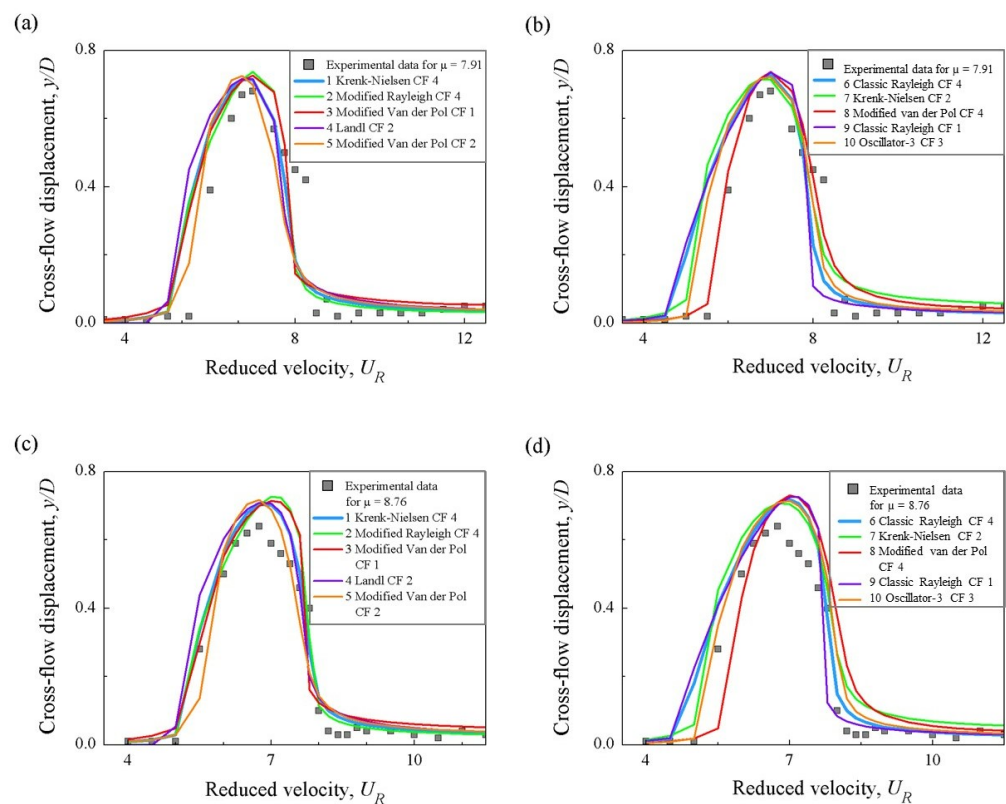
Figure 7. Cross-flow displacement amplitudes obtained by the one degree-of-freedom models in Appendix B, calibrated with the medium mass ratio: validation results for mass ratio 2.36 for oscillators 1–5 (**a**) and 6–10 (**b**), for mass ratio 3.68 for oscillators 1–5 (**c**) and 6–10 (**d**), for mass ratio 5.19 for oscillators 1–5 (**e**) and 6–10 (**f**). Experimental data for validation from [18]. Damping ratio $\xi = 0.006$, Reynolds number range 18,300–83,800.

Validation with high mass ratios data from the original series [18] in Figure 10 confirms the application range of these models up to approximately the mass ratio of 9.0. Model 8 may be considered relatively more accurate for the mass ratio 7.91, models 1, 2, 3 and 10 perform well for the mass ratio 8.76, according to Figure 10c,d, with some overestimation of the maximum observed displacements. This overprediction appears more pronounced for the mass ratio of 10.63 that is not shown in this paper, and models 3 and 5 provide the closest estimate for both peak slopes, capturing the overall bandwidth.
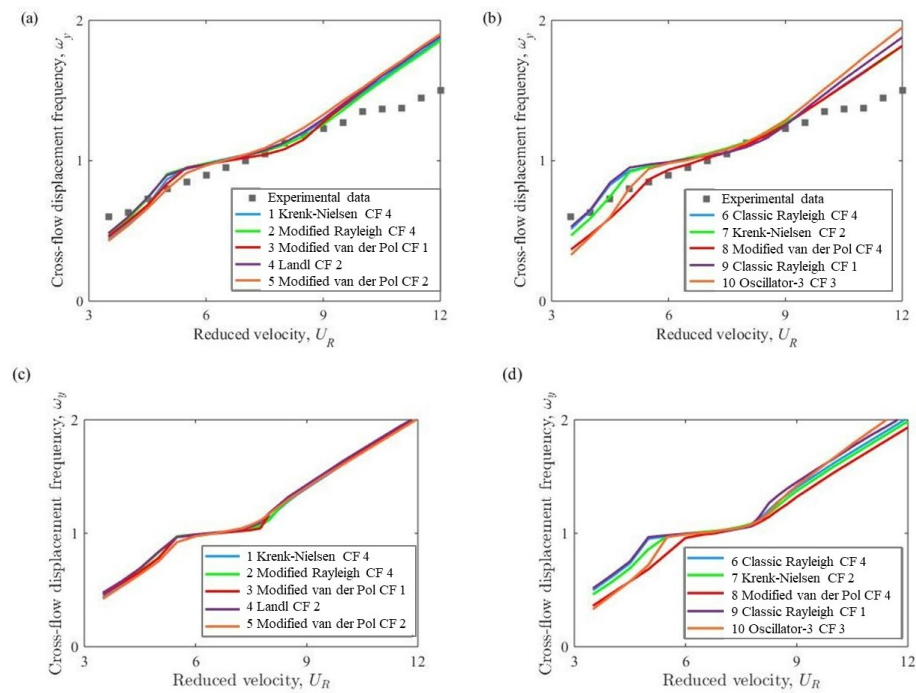
Figure 8. Cross-flow vibration frequencies obtained by the one degree-of-freedom models in Appendix B, calibrated with the medium mass ratio: results for mass ratio 2.36 for oscillators 1–5 (**a**) and 6–10 (**b**), and for mass ratio 6.54 for oscillators 1–5 (**c**) and 6–10 (**d**). Experimental data for validation from [18]. Damping ratio $\xi = 0.006$, Reynolds number range 18,300–83,800.

Figure 9. Cross-flow displacement amplitudes obtained by the one degree-of-freedom models in Appendix B, calibrated with the medium mass ratio: validation results for the mass ratio 3.01 with oscillators 1–5 (**a**) and 6–10 (**b**), and for the mass ratio 4.89 with oscillators 1–5 (**c**) and 6–10 (**d**). The experimental data are from [32]. The damping ratio is 0.008, and the Reynolds number range is 10,810–52,560.

Here, it is possible to indicate that model 7 with the Krenk–Nielsen damping and model 3 with the modified van der Pol damping may be considered as more qualitatively and quantitatively accurate for the original experimental set-up [18,32] for the mass ratios 2.36–10.63 and 3.68–8.76 respectively.

Considering the published experimental data in Figure 11 were obtained in two different laboratories [33,34], it may be confirmed that the coefficient *K* has to be adjusted to some parameters of the facility, possibly, boundary conditions and the aspect ratio, that are not fully accounted for in the basic mathematical formulation of the wake oscillator models. Hence, the coefficient *K* is assigned to 0, as in Section 4.1, in order to visualize capturing of the maximum amplitude and the lock-in range in the reduced velocity domain. Results in Figure 11a,b for the mass ratio 2.5 [33] confirm a reasonable quality of prediction provided by model 7 for the aspect ratio of 18. The accuracy of the lock-in modelling is generally higher for these models for the $L/D = 18$ then for $L/D = 24$, for the reasons discussed in Section 4.1.

Figure 10. Cross-flow displacement amplitudes obtained by the one degree-of-freedom models in Appendix B, calibrated with the medium mass ratio: validation results for mass ratio 7.91 for oscillators 1–5 (**a**) and 6–10 (**b**), and for mass ratio 8.76 for oscillators 1–5 (**c**) and 6–10 (**d**). Experimental data for validation from [18]. Damping ratio $\xi = 0.006$, Reynolds number range 18,300–83,800.

The data in Figure 11c,d for the mass ratio of 5.39 and the damping ratio of 0.1 from [34] demonstrate: (a) a wider lock-in bandwidth, (b) a mirrored similarity in the inclination of the initial and lower branches, (c) a scatter in the data for the lower branch, so it is not possible to predict definitely the maximum amplitudes expected in this range and (d) the amplitude jump following the maximum lock-in amplitude when the reduced velocity is increased. Therefore, the models calibrated with the set-up [18] for the medium mass ratio 6.54 are able to partially capture the lock-in occurrence. Models 4, 6 and 7 in Figure 11c,d may be considered as the closest qualitative and quantitative match to the overall peak shape, and models 4 and 7 allow an additional safety gap for the range of the initial branch occurrence.
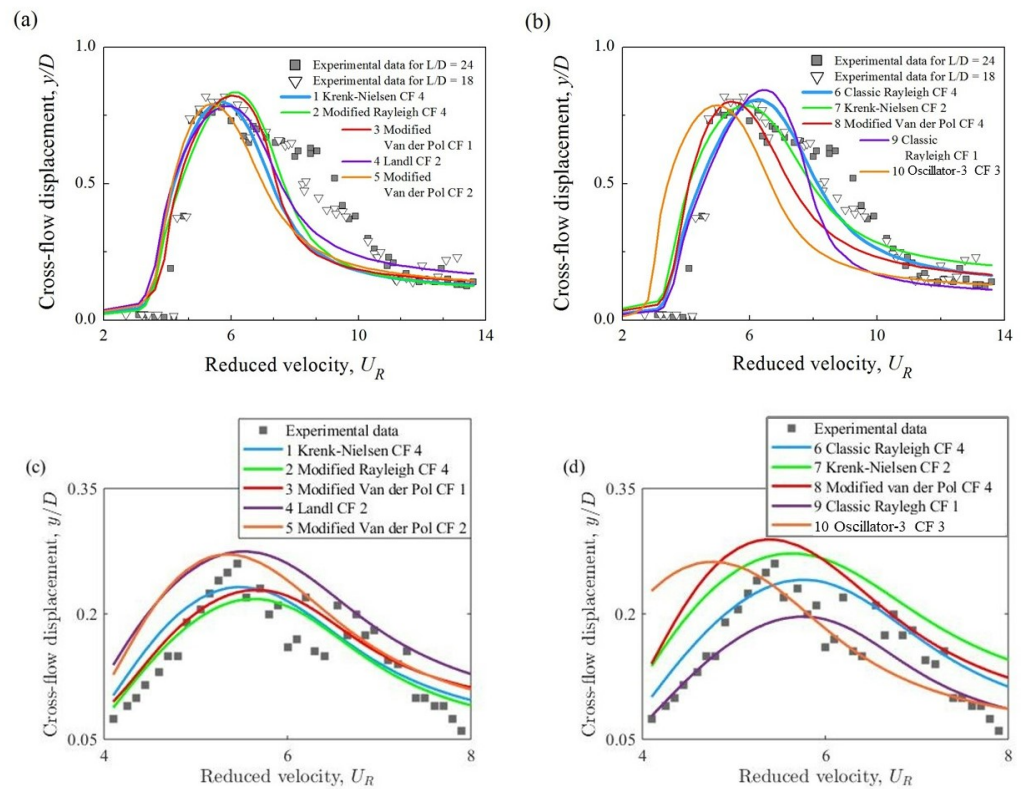
Figure 11. Cross-flow displacement amplitudes obtained by the one degree-of-freedom models in Appendix B, calibrated with the medium mass ratio: validation results for mass ratio 2.5 for oscillators 1–5 (**a**) and 6–10 (**b**), damping ratio of 0.005 and Reynolds number range 1320–6660 [33]; and for mass ratio 5.39 for oscillators 1–5 (**c**) and 6–10 (**d**), damping ratio of 0.1 and the Reynolds number interval of 19,890–39,050 [34]. The coefficient $K = 0$.

4.4. Discussion

The results reported above are summarized in Table 4 in comparison with results obtained in [28,36]. This summary indicates that tuned models with the largest application range between the mass ratio of 3.0 and 10.0 all belong to the category of rigid structure calibrated with the medium mass ratio. Here, the lock-in delay coefficient calibrated with the published data for a 2DOF rigid structure is applicable throughout several arrangements. However, the same empirical parameter has to be calibrated independently for each experimental arrangement when a 1DOF rigid structure is considered, for any mass ratio used for calibration. It is also worth noting a very limited application range of models calibrated with the high mass ratio when considering the dynamics of both 1DOF and 2DOF rigid structures.

The results in Section 4 provide sufficient evidence to recommend a general calibration approach: optimization of the semi-empirical models with the medium mass ratio while accounting for the features of the experimental arrangement, which may affect the emergence of lock-in phenomenon in terms of the reduced velocity. The validation with the published data of [18,32–34] points at some advantages of model 7 with the Krenk–Nielsen damping, calibrated with the medium mass ratio around 6.0. It may be also noted that the advantages of classic oscillators are more evident for the low mass ration cases, while new oscillators with extended damping may be more applicable to model shorter lock-ins, specific to the high mass ratio cases. Modified van der Pol, Krenk–Nielsen and both types of Rayleigh oscillators dominate the group of models optimized for the medium mass ratio, that has the most practical application range.

Table 4. Summary of calibrated models with low, medium and high mass ratios.

Mass Ratio	Borders of Application on the Same Set-Up in Terms of Mass Ratio	Borders of Application on Different Experimental Set-Ups in Terms of Mass Ratio
	1DOF	
Low	From 2 to 5, including lock-in delay coefficient	From 2 to 5, excluding lock-in delay coefficient
Medium	From 2-3 to 10-11, including lock-in delay coefficient	From 2 to 5, excluding lock-in delay coefficient
High	From 9 to 11, including lock-in delay coefficient	-
	2DOF	
Low	From 2 to 5, including lock-in delay coefficient	From 2 to 4, including lock-in delay coefficient
Medium	From 2 to 10, including lock-in delay coefficient	-
High	From 9 to 11, including lock-in delay coefficient	-

5. Conclusions

The present paper provides the summary of attempts to improve the accuracy of the VIV wake oscillator models, demonstrated on the example of transversally oscillating rigid cylinders mounted on elastic supports. This work is designed to fill the remaining gap in knowledge on the damping modification and optimization-based tuning of the semi-empirical wake oscillator models. The research constitutes a departure from the previous consideration of fluid oscillators suitable for one and two degrees-of-freedom rigid and flexible structures, by implementing a systematic, comprehensive calibration program for the three distinct mass ratios, instead of optimization for a single parameter set, and by consideration of more diverse damping terms.

The current study presents the case for the following major findings:

1. General recommendation to fine-tune the phenomenological models with the data for a medium mass ratio around 6.0, which allows capturing features of the lock-in response for an extended mass ratio range.
2. Advantageous use of the Krenk–Nielsen wake oscillator for cross-flow only VIV, compared to considered alternatives, including fluid oscillators with extended damping terms.
3. Confirmed necessity to account for the lock-in occurrence sensitivity in terms of the reduced velocity and the related Reynolds number to the specific features of experimental arrangements (often associated with the physical boundary conditions), that can be achieved by the introduction of the vortex shedding frequency tuning parameter, named the lock-in delay coefficient in this work.
4. General recommendation to model transversal-only oscillations with the models calibrated with the data for transverse VIV responses.

This study can be expanded in the future towards more advanced optimization techniques, further modifications to the basic mathematical formulation and the way to capture the dynamics for substantially different parametric ranges.

Appendix A. Optimization Settings

Table A1. Initial set of coefficients and their optimization constraints.

Parameter	Symbol	Initial Value	Lower Bound	Upper Bound
Initial lift coefficient	C_{L0}	0.3	0.01	3
Initial drag coefficient	C_{D0}	2	0.01	3
Cross-flow fluid damping parameter	ε_y	0.008	0.00001	2
Coupling coefficient	A_y	5	0	40
Fluid added mass coefficient	C_A	1	0.1	2
Lock-in delay coefficient	K	0	0	4

Appendix B. Optimized Coefficients

Table A2. Calibrated empirical parameters for wake oscillator models demonstrating lowest objective functions.

Fluid Oscillator	Objective Function	C_{L0}	C_{D0}	ε_y	A_y	C_A	K
Low Mass Ratio							
1. Classic Rayleigh	CF 3	0.75	2.25	0.006424	4.98	0.72	0.95
2. Classic Rayleigh	CF 4	0.80	2.23	0.008998	5.12	0.91	0.94
3. Classic van der Pol	CF 2	0.66	2.57	0.050361	7.48	1.50	1.17
4. Modified van der Pol	CF 1	0.74	1.41	0.358890, 0.547880	3.63	0.70	0.85
5. Modified Rayleigh	CF 3	0.47	1.81	0.009570, 0.399190	5.02	0.93	0.75
6. Modified van der Pol	CF 2	0.37	1.90	0.025168, 0.332520	5.98	0.65	1.06
7. Classic van der Pol	CF 1	0.88	1.80	0.295900	4.56	0.85	0.85
8. Modified Rayleigh	CF 4	0.84	2.25	0.022750, 0.223730	5.73	1.56	0.74
9. Krenk–Nielsen	CF 4	0.89	2.24	0.019919, 0.033541, 0.008071	5.11	0.78	1.01
10. Oscillator-4	CF 2	0.33	1.97	0.171950, 0.009893, 0.003658, 0.006449, 0.000965, 0.000248, 0.000068, 0.001285, 0.000001, 0.000018, 0.000009, 0.000003, 0.000019, 0.000118	11.10	0.69	1.22

Table A2. *Cont.*

Fluid Oscillator	Objective Function	C_{L0}	C_{D0}	ε_y	A_y	C_A	K
Medium Mass Ratio							
1. Krenk–Nielsen	CF 4	0.61	1.75	0.081990, 0.016313, 0.012551	5.49	1.12	1.34
2. Modified Rayleigh	CF 4	0.69	1.70	0.016162, 0.038019	5.14	0.95	1.22
3. Modified van der Pol	CF 1	0.58	1.22	0.367820, 0.696500	3.85	0.97	1.17
4. Landl	CF 2	0.67	1.90	0.008562, 0.009240, 0.008891	5.08	1.00	1.17
5. Modified van der Pol	CF 2	0.48	2.22	0.026508, 0.035601	6.28	1.13	1.40
6. Classic Rayleigh	CF 4	0.84	2.03	0.019019	5.28	0.87	1.04
7. Krenk–Nielsen	CF 2	0.86	2.03	0.177330, 0.088756, 0.036305	5.16	1.01	1.23
8. Modified van der Pol	CF 4	0.75	2.41	0.029661, 0.027102	4.65	1.12	1.70
9. Classic Rayleigh	CF 1	0.82	1.55	0.080460	4.71	1.19	0.96
10. Oscillator-3	CF 3	0.79	2.71	0.048490, 0.030415, 0.011808, 0.017899, 0.381170, 0.010902, 0.000964, 0.001431, 0.000161	9.42	1.68	2.12
High Mass Ratio							
1. Modified van der Pol	CF 2	0.39	1.42	0.057390, 0.075106	4.68	0.78	1.43
2. Krenk–Nielsen	CF 4	0.46	1.32	0.144630, 0.029808, 0.012312	5.53	1.30	1.44
3. Oscillator-3	CF 4	0.40	0.70	1.974500, 0.001903, 0.028620, 0.126120, 0.573010, 0.067134, 0.032737, 0.094681, 0.058406	19.31	0.75	2.32
4. Krenk–Nielsen	CF 2	0.62	2.04	0.050086, 0.045857, 0.014756	5.21	1.92	1.46
5. Landl	CF 2	0.64	1.74	0.000104, 0.000065, 0.014635	3.95	0.99	1.26
6. Modified Rayleigh	CF 3	0.50	1.65	0.007572, 0.023123	4.92	0.58	1.39
7. Classic Rayleigh	CF 4	0.67	2.04	0.010910	4.95	0.99	1.16
8. Modified van der Pol	CF 4	0.58	2.01	0.043130, 0.071177	5.10	0.77	1.28
9. Classic van der Pol	CF 3	1.12	1.45	0.654710	2.05	1.00	1.10
10. Oscillator-2	CF 3	0.37	2.51	0.009732, 0.010817, 0.000125, 0.014392, 0.013879, 0.000637	10.05	1.15	1.25

Appendix C. Experimental Case Parameters

Table A3. Parameters of experimental cases used for validation.

Parameter, Symbol (Units)		Value	
Experimental Set-Up	**Stappenbelt and O'Neill (2007) [32]**	**Franzini et al. (2009) [33]**	**Blevins and Coughran (2009) [34]**
Mass ratio, μ	3.01, 4.89	2.5	5.39
Damping ratio, ξ	0.008	0.005	0.1
Mass-damping ratio, $\mu\xi$	0.024, 0.039	0.0125	0.539
Griffin mass-damping ratio, $(\mu + C_A)\xi$	0.032, 0.047	0.0175	0.639
Maximum lock-in displacement amplitude, y/D	0.7, 0.62	0.82, 0.78	0.26
Diameter, D (m)	0.055	0.032	0.0635
Aspect ratio, L/D	8	18, 24	17.8
Natural frequency of structure, f_n (Hz)	1.215, 1.051	0.48	1.203

Table A3. *Cont.*

Parameter, Symbol (Units)		Value	
Experimental Set-Up	Stappenbelt and O'Neill (2007) [32]	Franzini et al. (2009) [33]	Blevins and Coughran (2009) [34]
Flow velocity interval, U (m/s)	0.20–0.96	0.042–0.209	0.31–0.61
Reynolds number interval, Re	10,810–52,560	1320–6660	19,890–39,050
Reduced velocity interval, U_R	3.4–14.3	2.7–13.6	4.10–8.05

References

1. Hartlen, R.; Currie, I. Lift-oscillator model of vortex-induced vibration. *J. Eng. Mech. Div.* **1970**, *96*, 577–591. [CrossRef]
2. Skop, R.; Griffin, O. A model for vortex-excited resonance response of bluff cylinders. *J. Sound Vib.* **1973**, *27*, 225–233. [CrossRef]
3. Landl, R. A mathematical model for vortex-excited vibrations of bluff bodies. *J. Sound Vib.* **1975**, *42*, 219–234. [CrossRef]
4. Skop, R.; Griffin, O. On a theory for the vortex-excited oscillations of flexible cylindrical structures. *J. Sound Vib.* **1975**, *41*, 263–274. [CrossRef]
5. Srinil, N.; Zanganeh, H. Modelling of coupled cross-flow/in-line vortex-induced vibrations using double Duffing and van der Pol oscillators. *Ocean Eng.* **2012**, *53*, 83–97. [CrossRef]
6. Krenk, S.; Nielsen, S. Energy balanced double oscillator model for vortex-induced vibrations. *J. Eng. Mech.* **1999**, *125*, 263–271. [CrossRef]
7. Ogink, R.; Metrikine, A. A wake oscillator with frequency dependent tuning coefficients for the modeling of VIV. In Proceedings of the ASME 2008 27th International Conference on Offshore Mechanics and Arctic Engineering, Estoril, Portugal, 15–20 June 2008; pp. 943–952.
8. Kurushina, V.; Pavlovskaia, E. Wake oscillator equations in modelling vortex-induced vibrations at low mass ratios. In Proceedings of the OCEANS 2017, Aberdeen, UK, 19–22 June 2017; pp. 1–6.
9. Shoshani, O. Deterministic and stochastic analyses of the lock-in phenomenon in vortex-induced vibration. *J. Sound Vib.* **2018**, *434*, 17–27. [CrossRef]
10. Wang, J.; Fu, S.; Baarholm, R.; Wu, J.; Larsen, C. Fatigue damage induced by vortex-induced vibrations in oscillatory flow. *Mar. Struct.* **2015**, *40*, 73–91. [CrossRef]
11. Facchinetti, M.; De Langre, E.; Biolley, F. Coupling of structure and wake oscillators in vortex-induced vibrations. *J. Fluids Struct.* **2004**, *19*, 123–140. [CrossRef]
12. Ogink, R.; Metrikine, A. A wake oscillator with frequency dependent coupling for the modeling of vortex-induced vibration. *J. Sound Vib.* **2010**, *329*, 5452–5473. [CrossRef]
13. Qu, Y.; Metrikine, A. A Wake Oscillator Model With Nonlinear Coupling for the VIV of Rigid Cylinder Constrained to Vibrate in the Cross-Flow Direction. In Proceedings of the ASME 2016 35th International Conference on Ocean, Offshore and Arctic Engineering, Busan, Korea, 19–24 June 2016; Volume 49934, p. V002T08A037.
14. Qu, Y.; Metrikine, A. A wake oscillator model with nonlinear coupling for the vortex-induced vibration of a rigid cylinder constrained to vibrate in the cross-flow direction. *J. Sound Vib.* **2020**, *469*, 115161. [CrossRef]
15. Nayfeh, A.; Owis, F.; Hajj, M. A model for the coupled lift and drag on a circular cylinder. In Proceedings of the ASME 2003 International Design Engineering Technical Conferences and Computers and Information in Engineering Conference, Chicago, IL, USA, 2–6 September 2003; pp. 1289–1296.
16. Barbosa, J.; Qu, Y.; Metrikine, A.; Lourens, E.M. Vortex-induced vibrations of a freely vibrating cylinder near a plane boundary: Experimental investigation and theoretical modelling. *J. Fluids Struct.* **2017**, *69*, 382–401. [CrossRef]
17. Qu, Y.; Metrikine, A. A single van der Pol wake oscillator model for coupled cross-flow and in-line vortex-induced vibrations. *Ocean Eng.* **2020**, *196*, 106732. [CrossRef]
18. Stappenbelt, B.; Lalji, F. Vortex-induced vibration super-upper response branch boundaries. *Int. J. Offshore Polar Eng.* **2008**, *18*, 99–105.
19. Postnikov, A. Wake Oscillator and CFD in Modelling of VIVs. Ph.D. Thesis, University of Aberdeen, Aberdeen, UK, 2016.
20. Srinil, N.; Opinel, P.A.; Tagliaferri, F. Empirical sensitivity of two-dimensional nonlinear wake–cylinder oscillators in cross-flow/in-line vortex-induced vibrations. *J. Fluids Struct.* **2018**, *83*, 310–338. [CrossRef]
21. Kinaci, O.; Lakka, S.; Sun, H.; Bernitsas, M. Effect of tip-flow on vortex-induced vibration of circular cylinders. *Ocean Eng.* **2016**, *117*, 130–142. [CrossRef]
22. Kurushina, V.; Pavlovskaia, E.; Postnikov, A.; Wiercigroch, M. Calibration and comparison of VIV wake oscillator models for low mass ratio structures. *Int. J. Mech. Sci.* **2018**, *142*, 547–560. [CrossRef]
23. Blevins, R.; Coughran, C. Experimental investigation of vortex-induced vibration in two-dimensions. In Proceedings of the Eighteenth International Offshore and Polar Engineering Conference, Vancouver, BC, Canada, 6–11 July 2008; International Society of Offshore and Polar Engineers: Mountain View, CA, USA, 2008.
24. Dahl, J.; Hover, F.; Triantafyllou, M. Two-degree-of-freedom vortex-induced vibrations using a force assisted apparatus. *J. Fluids Struct.* **2006**, *22*, 807–818. [CrossRef]

25. Jauvtis, N.; Williamson, C. The effect of two degrees-of-freedom on vortex-induced vibration at low mass and damping. *J. Fluid Mech.* **2004**, *509*, 23–62. [CrossRef]

26. Kurushina, V.; Pavlovskaia, E. Fluid nonlinearities effect on wake oscillator model performance. *Matec Web Conf.* **2018**, *148, 04002*. [CrossRef]

27. Kurushina, V.; Pavlovskaia, E.; Wiercigroch, M. VIV of flexible structures in 2D uniform flow. *Int. J. Eng. Sci.* **2020**, *150*, 103211. [CrossRef]

28. Kurushina, V.; Pavlovskaia, E.; Postnikov, A.; Franzini, G.R.; Wiercigroch, M. Modelling VIV of Transversally Oscillating Rigid Structures Using Nonlinear Fluid Oscillators. In *Nonlinear Dynamics of Structures, Systems and Devices*; Springer: Berlin/Heidelberg, Germany, 2020; pp. 379–387.

29. Postnikov, A.; Pavlovskaia, E.; Wiercigroch, M. 2DOF CFD calibrated wake oscillator model to investigate vortex-induced vibrations. *Int. J. Mech. Sci.* **2017**, *127*, 176–190. [CrossRef]

30. Govardhan, R.; Williamson, C. Modes of vortex formation and frequency response of a freely vibrating cylinder. *J. Fluid Mech.* **2000**, *420*, 85–130. [CrossRef]

31. Blevins, R. *Flow-Induced Vibration*; Van Nostrand Reinhold Co., Inc.: New York, NY, USA, 1990.

32. Stappenbelt, B.; O'Neill, L. Vortex-induced vibration of cylindrical structures with low mass ratio. In Proceedings of the Seventeenth International Offshore and Polar Engineering Conference, Lisbon, Portugal, 1–6 July 2007.

33. Franzini, G.; Fujarra, A.; Meneghini, J.; Korkischko, I.; Franciss, R. Experimental investigation of vortex-induced vibration on rigid, smooth and inclined cylinders. *J. Fluids Struct.* **2009**, *25*, 742–750. [CrossRef]

34. Blevins, R.; Coughran, C. Experimental investigation of vortex-induced vibration in one and two dimensions with variable mass, damping, and Reynolds number. *J. Fluids Eng.* **2009**, *131*, 101202. [CrossRef]

35. Govardhan, R.; Williamson, C. Mean and fluctuating velocity fields in the wake of a freely-vibrating cylinder. *J. Fluids Struct.* **2001**, *15*, 489–501. [CrossRef]

36. Kurushina, V. Fluid Nonlinearities for Calibrated VIV Wake Oscillator Models. Ph.D. Thesis, University of Aberdeen, Aberdeen, UK, 2018.